RSC Advances

PAPER

View Article Online
View Journal | View Issue

Cite this: *RSC Adv.*, 2016, **6**, 6266

Multi-substituted triazatruxene-functionalized pyrene derivatives as efficient organic laser gain media†

Ming Sang,[a] Sizhen Cao,[a] Jianpeng Yi,[a] Jinjin Huang,[a] Wen-Yong Lai*[ab] and Wei Huang*[ab]

A set of pyrene derivatives substituted with multiple triazatruxene at the 1, 6- and 1, 3, 6, 8-positions, namely **Py-2TAT** and **Py-4TAT**, was synthesized and characterized. Their thermal, photophysical, and electrochemical properties were investigated in comparison with those of the pyrene and triazatruxene units to explore the relationship between the molecular architectures and corresponding properties. It is found that introducing a triazatruxene unit onto the rigid pyrene chromophore can effectively depress the crystalline nature of the pyrene and triazatruxene units, which endow the resulting materials with improved morphology properties, enhanced thermal stabilities, and favorable solution processiblity. Particularly, due to the integration of triazatruxene functional units, the resulting materials exhibit high-lying HOMO energy levels that are well matched with that of the PEDOT:PSS/ITO anode, leading to an improved hole-injection property. Solution-processed non-doped films exhibited prominent amplified spontaneous emission (ASE) and lasing characteristics. Low ASE thresholds of 150 nJ per pulse (1.4 kW cm^{-2}) at 508 nm for **Py-2TAT** and 450 nJ per pulse (4.1 kW cm^{-2}) at 530 nm for **Py-4TAT** were recorded. Consequently, one-dimensional (1D) distributed feed-back (DFB) lasers with low lasing threshold of 21 nJ per pulse (8.6 kW cm^{-2}) was demonstrated. The selection of different combinations of grating periods and film thicknesses has provided the opportunity to fine tune the lasing wavelength of the DFB lasers in the range of 484–556 nm. The results indicated that construction of multi-substituted triazatruxene-pyrene architectures was beneficial to improving the electrical properties and thermal stabilities without largely sacrificing the optical properties, manifesting the potential of triazatruxene-functionalized pyrenes as efficient gain media for electrically pumped organic lasers.

Received 1st December 2015
Accepted 24th December 2015

DOI: 10.1039/c5ra25530a

www.rsc.org/advances

Introduction

Great progress has been made, particularly in the past decade, in the search for organic semiconductor materials with attractive optoelectronic properties for applications in the next generation of optoelectronic devices.[1,2] Recently, solution-processed organic emitters with desirable optical and electrical properties have attracted much attention for applications in organic light-emitting diodes (OLEDs)[3–5] and organic lasers.[6–8] To date, despite significant progress has been achieved in OLEDs, electrically pumped organic lasers have not been realized yet.[9–14] In this context, the rational design and synthesis of novel organic emitters with excellent optical gains, high carrier mobility and enhanced thermal stability are highly demanded. Most of the existing organic emitters generally suffer from their intrinsic low carrier mobility despite the higher optical gains and lower threshold energy relative to their inorganic counterparts.[8] Generally, high carrier mobility and high luminous efficiency are contradictory for organic emitters. Thus, a search for new efficient organic emitters as organic laser gain media with superior optical and electrical properties and a better understanding of the relationship between molecular structures and device properties are highly required.

As far as we are concerned, high luminous efficiency is an important prerequisite to obtain high optical gains, which can be achieved by polycyclic aromatic units such as fluorene,[15–17] anthracene[18–20] and pyrene.[21–23] Among these, pyrene has stood out as a promising building block because of its high photoluminescence quantum yields (PLQYs), high charge carrier mobility and excellent thermal stability.[23] However, pyrene itself and its derivatives normally tend to aggregate, resulting in red-shifted emission and low PLQYs in solid states.[21–23] The pyrene

[a]*Key Laboratory for Organic Electronics and Information Displays (KLOEID) & Institute of Advanced Materials (IAM), Jiangsu National Synergetic Innovation Center for Advanced Materials (SICAM), Nanjing University of Posts & Telecommunications, 9 Wenyuan Road, Nanjing 210023, China . E-mail: iamwylai@njupt.edu.cn*

[b]*Key Laboratory of Flexible Electronics (KLOFE) & Institue of Advanced Materials (IAM), Jiangsu National Synergetic Innovation Center for Advanced Materials (SICAM), Nanjing Tech University (NanjingTech), 30 South Puzhu Road, Nanjing 211816, China . E-mail: wei-huang@njtech.edu.cn*

† Electronic supplementary information (ESI) available. See DOI: 10.1039/c5ra25530a

aggregation can be suppressed by introducing bulky groups and star-shaped structures.[23] From a structural perspective, the facile chemical modification of the pyrene structure makes it possible to induce novel molecular architectures *via* introducing various substitutions, thus varying corresponding optoelectronic properties. For instance, Krotkus *et al.* developed a series of pyrenyl-disubstituted fluorene and carbazole compounds which demonstrated promising ASE performance with low ASE threshold (down to 20 kW cm^{-2}) with pyrene derivatives dispersed in the inert polystyrene matrix at a rather large optimal (3–5 wt%) chromophore concentration.[24] Although the electrical properties can be fine modulated *via* incorporating electroactive carbazole units onto pyrene cappers structures, the optimal performance was achieved in a blend system.

Triazatruxene (**TAT**) comprising three overlapping carbazole fragments has attracted increasing recent interests.[25–27] High mobility has been recorded from triazatruxene derivatives.[28] Ziessel *et al.* developed a series of monosubstituted triazatruxenes dyes which showed large fluorescence quantum yields and electrochemical properties as well as high hole mobility.[29] Meanwhile, it is also reported that the thermal stability of the compounds can be greatly enhanced by incorporating triazatruxene in the molecular structure.[30,31] In our previous work, we have developed a novel series of monodisperse star-shaped conjugated macromolecules based on truxene or triazatruxene core with oligofluorene arms, which exhibited promising electroluminescence, optical gain, and lasing performance.[31–36]

As a matter of fact, facile solution processibility of polymers is significant to reduce the concentration quenching in the device fabrication. In contrast to polymers, small molecules have demonstrated great advantages as they can possess well-defined structures and high purity. Combined with both advantages mentioned above, monodisperse conjugated oligomers have been proven to be the most potential system, which provide a valuable platform to clarify the relationship between structures and properties. Furthermore, these oligomers can be easily fabricated into the amorphous and homogeneous films, showing high morphological stability in the device manufacture. Therefore, multifunctional compounds based on pyrene moieties have been developed and studied for the state-of-art, solution-processed OLEDs. Recently, Qin *et al.* developed monodisperse pyrene derivatives containing four peripheral triphenylene dendrons and triphenylamine surface groups which can be used as blue emitters with high luminance and high operational stability.[37]

Inspired by the promising characteristics of pyrene and triazatruxene, we intended to introduce the two building blocks into a monodisperse star-shaped architecture with the aim to accomplish high electrical properties and thermal stabilities while maintaining favorable optical characteristics. Thus, a set of compounds which integrated the triazatruxene functional units onto the planar rigid pyrene chromophore at 1, 6- and 1, 3, 6, 8-positions (**Py-2TAT** and **Py-4TAT**) were designed and synthesized. Introduction of the alkyl chain onto the triazatruxene moiety enabled the resulting molecules to be solution processible. The thermal, photophysical, and electrochemical properties of **Py-2TAT** and **Py-4TAT** were investigated to explore the relationship between the molecular architectures and properties. The lasing wavelength of the distributed feed-back (DFB) lasers can be fine-tuned in the range of 484–556 nm *via* an appropriate choice of grating periods and film thicknesses. Consequently, for **Py-2TAT**, promising lasing performance with low ASE threshold of 150 nJ per pulse (6.8 μJ cm^{-2}) and low lasing threshold of 21 nJ per pulse (8.6 kW cm^{-2}) was demonstrated.

Results and discussion

Synthesis and characterization

Synthesis of triazatruxene-functionalized pyrene derivatives **Py-*n*TAT** is depicted in Scheme 1. 1,3,6,8-Tetrabromopyrene was synthesized according to the ref. [38]. 1,6-Dibromopyrene was purchased from J&K Scientific Ltd. China. Triazatruxene (**TAT**) was prepared by reported methods[39] and bromination of triazatruxene with *N*-bromosuccinimide (NBS) was synthesized according to the ref. [27]. Pyrene derivatives substituted with triazatruxene at the 1,6-(**Py-2TAT**) and 1,3,6,8-positions (**Py-4TAT**) were efficiently obtained by consecutive two-step synthesis through boronic pinacol esters of monobrominated triazatruxene followed by mutiple Suzuki coupling reactions.[36] The molecular structures and purities were adequately confirmed by ^{1}H and ^{13}C NMR spectroscopy, and MALDI-TOF mass spectrometry.

Thermal and morphology properties

Thermal stabilities of triazatruxene-substituted pyrene derivatives were estimated using thermogravimetric analysis (TGA) and differential scanning calorimetry (DSC), respectively. As shown in Fig. S1 and S2,† **Py-2TAT** and **Py-4TAT** exhibited good thermal stability with 5% weight loss decomposition temperature (T_d) up to 378 °C and 376 °C, respectively. The glass transition temperature (T_g) for **Py-4TAT** is 89 °C, which is higher than **Py-2TAT** (57 °C). The thermal characteristics of the resulting molecules are summarized in Table 1. To identify the crystallinity of **Py-*n*TAT** materials, wide-angle X-ray diffraction (WXRD) was performed. From the WXRD patterns (Fig. 1), we clearly observe a transition from a polycrystalline to an amorphous state by increasing the triazatruxene substitutions from **Py-2TAT** to **Py-4TAT**. In contrast, sharp peaks for the pyrene core (**Py**) and triazatruxene unit (**TAT**) were observed. It is implied that integration the triazatruxene unit onto rigid pyrene chromophore can depress the crystalline nature of pyrene and triazatruxene units.

Atomic force microscopy (AFM) images of the compounds were recorded on spectrosil substrates to investigate their morphological stability (Fig. 2). The thin films were prepared by spin-coating without any treatment. The thin film had a smooth surface morphology with a root-mean-square (RMS) roughness of 0.475 for **Py-2TAT** and 0.546 nm for **Py-4TAT**, respectively. For comparison, the films of **TAT** and **Py** were prepared, which showed rather coarse surface due to their high crystallinity. The trends are consistent with the XRD analysis. The results indicate

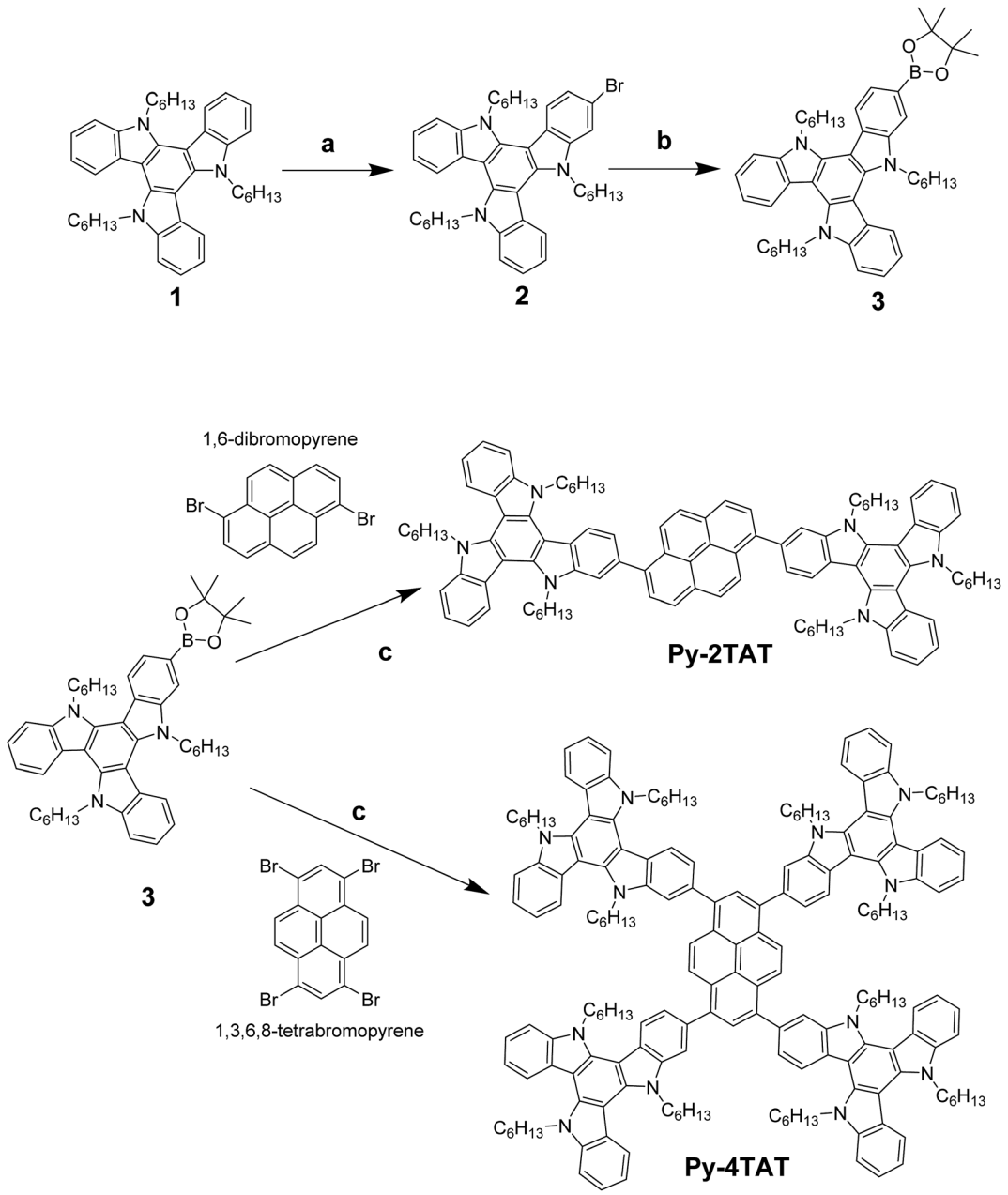

Scheme 1 Synthetic routes towards Py-*n*TAT. Reagents and conditions: (a) NBS, DMF, acetonitrile, 0 °C; (b) bis(pinacolato)diboron, Pd(dppf)Cl_2, KOAc, 1,4-dioxane, 100 °C; (c) $Pd(PPh_3)_4$, K_2CO_3, H_2O, 1,4-dioxane, 100 °C.

that construction of multi-substituted triazatruxene-pyrene molecular architectures is helpful for improving the amorphous properties and film-forming properties that would largely facilitate the fabrication of much more homogeneous thin films by solution processing, which is desirable for organic optoelectronic devices.

Photophysical properties

The photophysical properties of **TAT**, **Py** and **Py-*n*TAT** were measured by UV-vis absorption and photoluminescence (PL) spectra in THF and in thin films (Fig. 3). **TAT** and **Py** show well-resolved absorption in dilute THF, whereas their absorption spectra in the thin film exhibit a strong π–π* transition with a broad tail at low energy, which might be related to excimers or aggregates of the rigid monomer molecules. In the film states, PL spectra of **TAT** and **Py** are relatively broader and red-shifted compared with those recorded in THF. Additionally, a weak shoulder at near 450 nm for **TAT** and a strong fluorescence band around 460 nm for **Py** can also be observed, which are attributed to the emission from aggregates formed by the rigid monomer molecules in the solid states.

Py-*n*TAT exhibit prominent short and long wavelength absorption peaks (see Fig. 3c and d and Table 1). The shorter wavelength bands at 300–350 nm may originate from the

Table 1 Thermal and photophysical properties of Py-*n*TAT

Compound	T_g[a], °C	T_d[b], °C	λ_{abs}, nm (THF)	ε, [10^5 L mol^{-1} cm^{-1}] (log ε)	λ_{PL}, nm (THF)	λ_{abs}, nm (film)	λ_{PL}, nm (film)	PLQY[c]
Py-2TAT	57	378	302, 399	0.9 (4.95), 0.29 (4.46)	487	322, 413	487	0.16
Py-4TAT	89	376	304, 417	2.21 (5.34), 0.47 (4.67)	493	322, 427	514	0.66

[a] Scan rate 10 °C min^{-1}, N_2 atmosphere. [b] Heating rate 10 °C min^{-1}, N_2 atmosphere. [c] Fluorescence quantum yields in solid state films, measured on quartz plates using an integrating sphere.

triazatruxene moiety, while the longer bands at 350–480 nm are ascribed to the π–π* transition of the pyrene moiety. In THF solution, **Py-4TAT** shows red-shifted wavelength absorption maxima (λ_{max}) at 304 nm and a shoulder peak at 417 nm in comparison to **Py-2TAT** (λ = 302 and 399 nm, respectively), owing to its slightly more extended conjugation lengths. In the film state, both **Py-2TAT** and **Py-4TAT** exhibit two characteristic absorption peaks, which are relatively red-shifted from those recorded for THF solutions. Both compounds show green emissions with the peaks at 487 and 493 nm for **Py-2TAT** and **Py-4TAT**, respectively. The film PL spectra for **Py-2TAT** are almost identical to those obtained in solution, while **Py-4TAT** displays emission peak at 514 nm, which are red-shifted about 21 nm relative to its solution spectra, indicating weak intermolecular interactions in thin films. Apparently, constructing multi-substituted architectures can effectively depress the π-stacking/aggregation tendency of the planar **TAT** units and the rigid **Py** core structure in the solid state. Photoluminescence quantum yields (PLQY) of these materials in the solid states measured on quartz plates using an integrating sphere are 0.16 for **Py-2TAT** and 0.66 for **Py-4TAT**. As a result, PLQY of tetra-substituted pyrene compound **Py-4TAT** is much higher than that of disubstituted pyrene compound **Py-2TAT**, showing a comparable level to other tetrasubstituted pyrene derivatives but with more simple synthetic architectures.[40,41]

Fluorescence transients of **TAT**, **Py** and **Py-*n*TAT** were investigated to get further insight into the excited state relaxation processes. The transients measured at the fluorescence band maxima of the studied compounds in the dilute solutions and the neat films are presented in Fig. S3 and S4.† The emission decays of **Py** and **TAT** are recorded by employing two discrete exponentials in THF with excellent fits (Table S1†). In THF solution, single exponential decays are evident for both **Py-2TAT** and **Py-4TAT** with excited state lifetimes (τ) of 3.32 and 3.96 ns, respectively. The decay times are similar to those reported for 1-pyrene substituted derivatives[24,42,43] and pyrene-cored dendrimers[44,45] in the monomeric state.

The fluorescence transients of the neat films were fairly well described by using a double exponential decay model yielding two decay components with different fractional intensities, that is, different contributions to the overall decay profile, pointing out several different origins of the radiative transitions. In the films, **Py-*n*TAT** compounds possess two lifetime components, probably originating from their similar fluorescent backbones. The fast decay component (τ_1) of the neat films is less than 1 ns (0.83 ns for **Py-2TAT** and 0.98 ns for **Py-4TAT**), which has a dominant contribution (fractional intensity 69–72%) in their fluorescence decay dynamics. The fast component may result

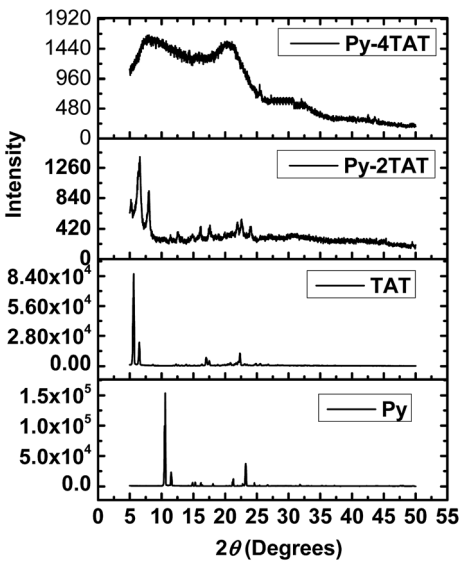

Fig. 1 WAXD patterns (5–50°) of **TAT**, **Py** and **Py-*n*TAT** powders. All samples were tested under the same conditions, and each pattern was demonstrated at its original intensity.

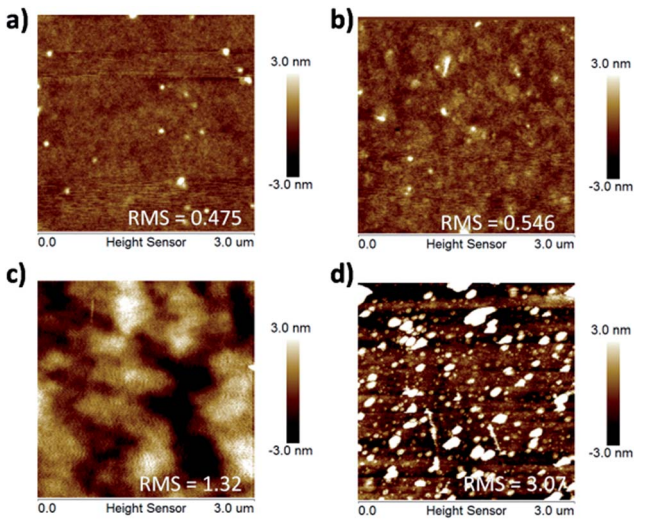

Fig. 2 AFM topographic images of (a) **Py-2TAT**, (b) **Py-4TAT**, (c) **TAT** and (d) **Py**.

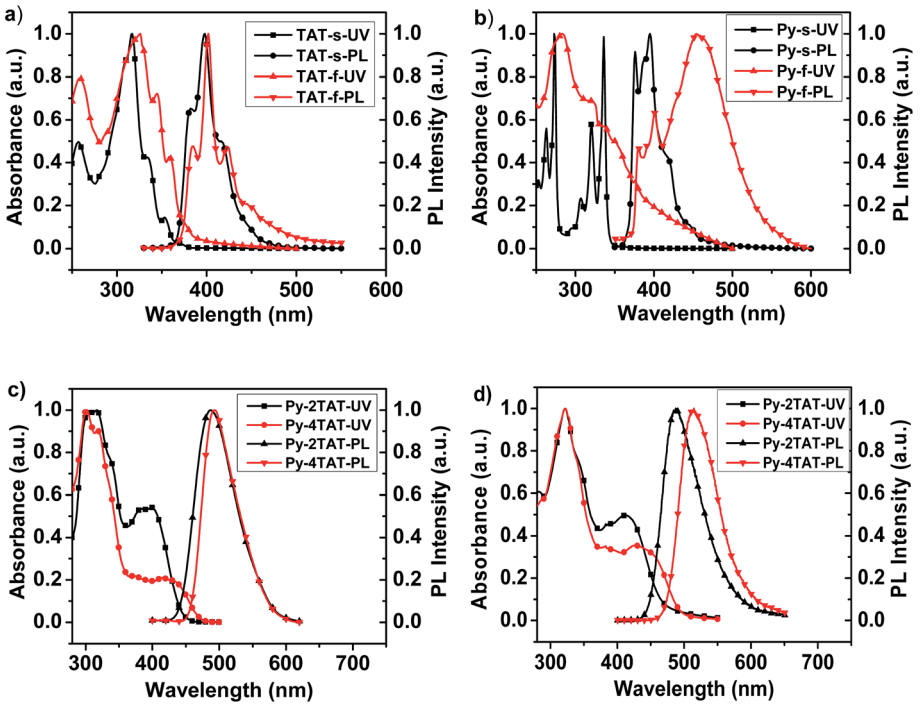

Fig. 3 Normalized absorption and emission spectra of (a) TAT, (b) Py, and Py-*n*TAT in (c) THF and (d) film states.

from exciton migration, and/or the migration-induced exciton quenching.[24] Bearing in mind the formation of molecular aggregates in the neat films, as evidenced from their fluorescence bands, the slow relaxation component with τ_2 (2.38 ns for **Py-2TAT** and 2.55 ns for **Py-4TAT**) can be attributed to the aggregated states.[24] In addition, Table S2† shows the average PL lifetimes (τ) for **Py-2TAT** and **Py-4TAT** are 1.30 and 1.42 ns, respectively. Reduced χ^2 values, which are used together with weighted residuals as the goodness-of-fit criteria, do not exceed 1.2, ensuring a reliable description of the experimental data.

Electronic and electrochemical properties

The molecular structures of the **Py-*n*TAT** were optimized using density functional theory (DFT) method (B3LYP) with 6-31G (d) basis set by GAUSSIAN 09. For simplicity and clarity, the lengthy alkyl chains were replaced by methyl in the model structures. It was assumed that such a change would not affect the calculation results for relevant discussion here. The optimized geometries and calculated frontier orbitals of **Py-2TAT** and **Py-4TAT** are depicted in Fig. S5.† The highest occupied molecular orbital (HOMO) and the lowest unoccupied molecular orbital (LUMO) values calculated with B3LYP/6-31G(d,p) level for **Py-*n*TAT** are summarized in Table 2.

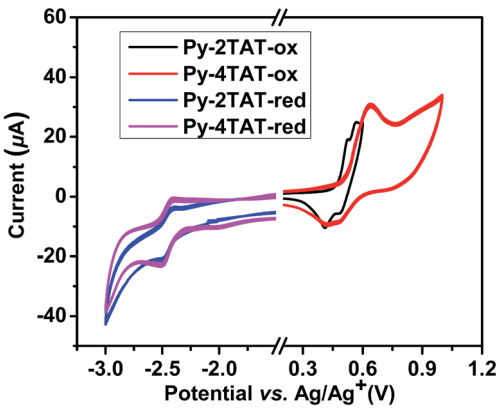

Fig. 4 CVs of Py-*n*TAT.

Table 2 Cyclic voltammetric [a] and DFT calculated data of Py-*n*TAT

Compound	E_{ox}[b], (V)	E_{red}[b], (V)	E^{cv}_{HOMO}[c], (eV)	E^{cv}_{LUMO}[c], (eV)	E_g^{opt}[d], (eV)	E^{cal}_{HOMO}[e], (eV)	E^{cal}_{LUMO}[e], (eV)	E_g^{cal}[e], (eV)
Py-2TAT	0.46	−2.34	−5.17	−2.37	2.79	−4.78	−1.46	3.32
Py-4TAT	0.50	−2.39	−5.21	−2.32	2.63	−4.58	−1.59	2.99

[a] Cyclic voltammogram curves of drop-coated films measured in 0.1 M Bu_4NPF_6 acetonitrile solution at a scan rate of 50 mV s^{-1} at room temperature (*versus* Ag/Ag^+). [b] Onset oxidation potentials *versus* Ag/Ag^+. [c] Estimated from the onset oxidation and reduction potential by using $E^{cv}_{HOMO} = -e(E_{ox} + 4.71\ V)$ and $E^{cv}_{LUMO} = -e(E_{red} + 4.71\ V)$. [d] E_g^{opt} (optical gap) calculated from the onset of absorption used the formula: $E_g^{opt} = 1240/\lambda_{onset}$. [e] HOMO and LUMO calculated with B3LYP/6-31G(d,p) level.

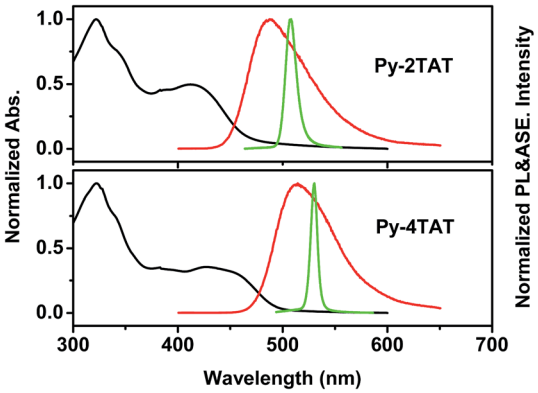

Fig. 5 Absorption, emission and ASE spectra (excited at 355 nm) of Py-*n*TAT films.

The optimized geometries show that the pyrene core and triazatruxene substitutions are significantly twisted, rendering the chair-shaped **Py-2TAT** molecule and bowl-shaped **Py-4TAT** molecule with a twisted nonplanar structure. The different numbers of triazatruxene attached to the pyrene core result in different molecular packing. Obviously, **Py-4TAT** causes more pronounced steric hindrance effects and, thus, is more favorable for preventing molecular aggregation in the solid state than **Py-2TAT**. Meanwhile, this assumption has been confirmed by thermal and morphology analysis as mentioned above. For **Py-2TAT**, the LUMO is dominated by the pyrene unit, while the HOMO is mainly delocalized on the whole molecule. However, for **Py-4TAT**, an obvious overlap exists between the HOMO and LUMO, indicating that delocalization occurs across over the pyrene core structure.

The electrochemical characteristics of **Py-*n*TAT** were studied by cyclic voltammetry (CV) to further reveal the electronic properties. The data are collected in Table 2, in comparison with those calculated with B3LYP/6-31G (d). As shown in Fig. 4, the onsets of the oxidation potentials were found to be 0.46 and 0.56 V for **Py-2TAT** and **Py-4TAT**, respectively. In Table 2, the HOMOs of **Py-2TAT** and **Py-4TAT** are calculated to be −5.17 and −5.21 eV, respectively. The LUMO levels are deduced to be −2.37 and −2.32 eV from the reduction potentials. Noticeably, it is found that integration of triazatruxene functional units onto the pyrene core endows the materials with HOMO levels that are well matched with that of the poly(3,4-ethylenedioxythiopene):poly (styrenesulfonate) (PEDOT:PSS)/ITO anode (−5.20 eV),[46] leading to a significantly improved hole-injection property. Based on the red edge of the longest absorption wavelength for the solid-state sample, the optical band gaps (E_g) of **Py-2TAT** and **Py-4TAT** were estimated to be 2.79 and 2.63 eV, respectively. All the results indicate that DFT calculations follow similar trends as revealed in the CV study.

Amplified spontaneous emission

To reveal the optical gain properties, amplified spontaneous emission (ASE) properties of the triazatruxene-functionalized pyrene compounds **Py-2TAT** and **Py-4TAT** were examined without utilization of external resonators or patterned distributed feedback grating structures. As a simple and appropriate technique, ASE measurements are widely applied to compare the performance of different materials for lasing application excluding effects of resonant cavity.[6,47]

When the sample was pumped at high excitation densities, we observed ASE from the edge of the **Py-2TAT** film, with a line-narrowed spectrum (Fig. 5) peaked at 508 nm, close to the 0–1 vibronic peak of the PL emission. This is consistent with a quasi-four-level vibronic system allowing low-threshold operation.[7] Simultaneously, ASE from the edge of the **Py-4TAT** film was seen at 530 nm. Fig. 6 shows the full-width at half-maximum (FWHM) line width of the emission spectrum and relative output power as a function of the pump intensity. According to the results, the FWHM of **Py-2TAT** has dropped dramatically from 66 nm to 12 nm when pumped above a threshold intensity E_{th}^{ASE} of 150 nJ (1.4 kW cm^{-2}). As shown in the inset of Fig. 6a, the output emission is amplified when the energy of pumped laser pulse is above the threshold. In Fig. 6b,

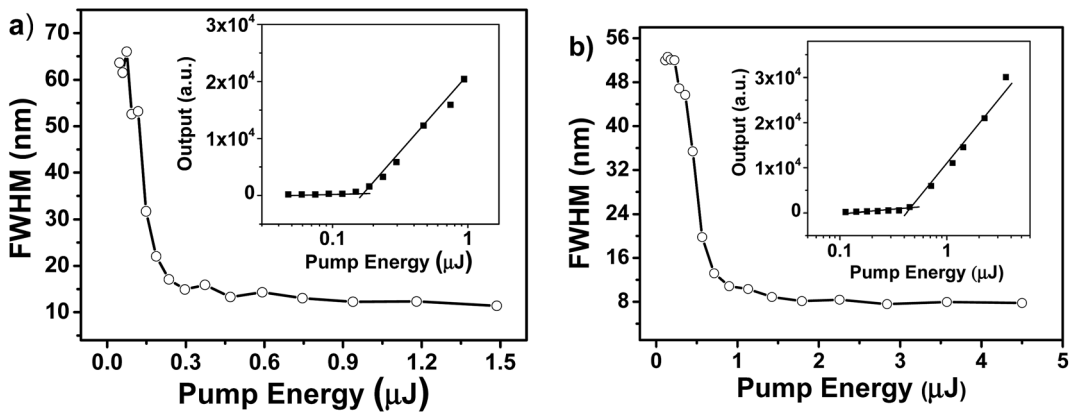

Fig. 6 (a) The dependence of the FWHM of the emission spectra on the pump energy density for a Py-2TAT film of (188 ± 5) nm thickness; (inset) the total emission intensity from the edge of the same Py-2TAT waveguide *versus* pump energy density. (b) The dependence of the FWHM of the emission spectra on the pump energy density for a Py-4TAT film of (250 ± 5) nm thickness; (inset) the total emission intensity from the edge of the same Py-4TAT waveguide *versus* pump energy density.

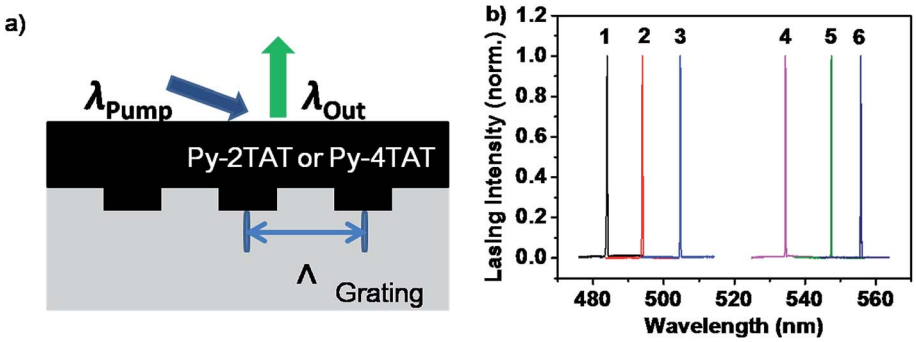

Fig. 7 (a) Schematic diagram of the DFB laser structure. (b) Laser emission spectra for 1D order.

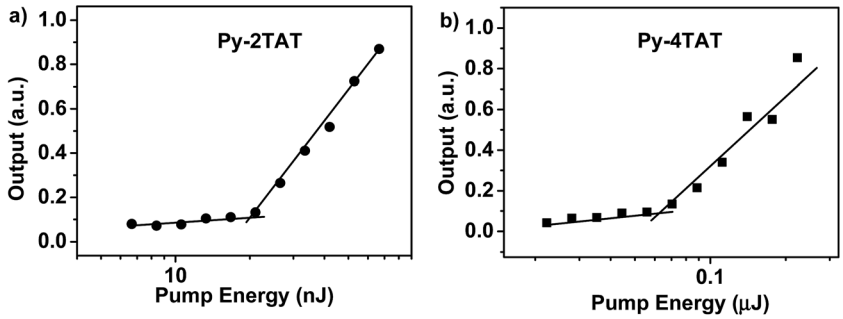

Fig. 8 (a) **Py-2TAT** laser threshold of 21 nJ (8.6 kW cm^{-2}) at the emission wavelength of 494 nm. (b) **Py-4TAT** laser threshold of 60 nJ (24.5 kW cm^{-2}) at the emission wavelength of 547 nm.

Py-4TAT has the same ASE characteristics as **Py-2TAT**, while the FWHM of the emission spectrum of **Py-4TAT** decreases to 8 nm with a line-narrowed spectrum peaked at 530 nm and a threshold intensity of 450 nJ (4.1 kW cm^{-2}). Therefore, **Py-2TAT** has the lowest E_{th}^{ASE}, which is comparable to other pyrene derivatives[24] and much better than perylene derivatives (15–20 kW cm^{-2}) under analogous conditions.[48–50] It is worthwhile to note that non-doped organic lasers have great advantages over small molecules because they suffer little from the concentration quenching.

Organic lasing properties

One-dimensional (1D) distributed feedback (DFB) lasers were fabricated by spin-coating thin films of **Py-*n*TAT** on top of etched nano-printed 1D gratings (Fig. 7a). Their performances were tested under the same pulsed optical excitation as used for ASE studies. Above the laser threshold, the surface-emission spectrum has narrowed to a single peak of line width 0.1–0.3 nm line width. Typical laser spectra are shown in Fig. 7b for various lasers. By selecting different combinations of grating periods and film thicknesses, the lasing wavelength of the DFB lasers could be fine tuned in the range of 484–505 nm and 535–556 nm for **Py-2TAT** and **Py-4TAT**, respectively. For a grating with period of 290 nm, fill factor of 50%, and etch depth of 30 nm, low lasing threshold of 21 nJ per pulse (8.6 kW cm^{-2}) was achieved for a laser based on **Py-2TAT** operating at 494 nm with a film thickness of 125 nm (Fig. 8a). For **Py-4TAT** (Fig. 8b), lasing threshold values of 60 nJ per pulse (24.5 kW cm^{-2}) by using a grating with period of 350 nm, fill factor of 50%, and etch depth of 30 nm were recorded, which was 3-fold higher than that of **Py-2TAT**. Consequently, these lasing results match well with the ASE results and suggest that **Py-2TAT** exhibits superior ASE and lasing characteristics. The results suggest more bulky triazatruxene functional units integrated onto the pyrene core are detrimental to optical gain (Table 3).

Table 3 ASE and lasing properties of Py-*n*TAT

Compound	λ_{ASE}[a] (nm)	E_{th}^{ASE} (nJ per pulse)	FWHM[b] (nm)	λ_{laser} (nm)	E_{th}^{laser} (nJ per pulse)	E_{th}^{laser} (kW cm^{-2})@λ_{laser} (nm)
Py-2TAT	508	150	12	484–505	21	8.6@494
Py-4TAT	530	450	8	535–556	60	24.5@547

[a] ASE peak wavelength. [b] Minimal full width at half-maximum of the ASE band.

Py-*n*TAT DFB lasers with different grating periods. For **Py-2TAT**, lasing from 484 (1), 494 (2) and 505 nm (3) are from 280, 290 and 300 nm period 1D grating, respectively. For **Py-4TAT**, lasing from 535 (4), 547 (5) and 556 nm (6) are from 340, 350 and 360 nm period 1D grating, respectively. Film thicknesses: 125 nm for **Py-2TAT** and 100 nm for **Py-4TAT**.

Conclusions

In summary, we have designed and synthesized a set of new pyrene derivatives substituted with triazatruxene at 1,6- and 1, 3, 6, 8-positions. The combination of pyrene and triazatruxene units into a monodisperse multi-substituted molecular architecture results in improved thermal stabilities, facile solution processability, and enhanced electrical properties while maintaining promising optical gain properties. Specifically, integration of triazatruxene functional units onto the pyrene core endows the materials with high-lying HOMO energy levels that are well matched with that of the PEDOT:PSS/ITO anode (−5.20 eV), leading to an improved hole-injection property. Non-doped organic lasers based on these materials by solution processing exhibit highly efficient luminescence and promising lasing characteristics. Meanwhile, the selection of different combinations of grating periods and film thicknesses has provided the opportunity to fine tune the lasing wavelength of the DFB lasers in the range of 484–556 nm. In this way, low ASE threshold of 150 nJ per pulse (1.4 kW cm^{-2}) and low lasing threshold of 21 nJ per pulse (8.6 kW cm^{-2}) were demonstrated for triazatruxene-disubstituted pyrene derivatives. The results indicated that such a design strategy was beneficial to improving the electrical properties and thermal stabilities without largely sacrificing the optical properties, manifesting the great potential of triazatruxene-functionalized pyrenes as efficient gain media for electrically pumped organic lasers.

Experimental section

Materials

All the reagents used were purchased from Sigma-Aldrich, J&K or Xiya Reagent (China). When necessary, solvents and reagents were purified using standard procedures.

Characterization

NMR spectra were recorded on a Bruker Ultra Shield Plus 400 MHz NMR (^{1}H: 400 MHz, ^{13}C: 100 MHz). The matrix assisted laser desorption ionization time of flight mass spectroscopy (MALDI-TOF MS) measurements were carried out with a Shimadzu AXIMA-CFR mass spectrometer. UV-visible absorption spectra were recorded on a Shimadzu UV-3600 UV-vis-NIR spectrophotometer. Photoluminescence (PL) spectra were measured using a RF-5301 PC spectrofluorophotometer. Lifetimes were measured using an Edinburgh FLSP920 lifetime spectrometer with a 375 nm laser (typical pulse width: 55 ps; pulse repetition frequencies: 20 MHz); the fluorescence quantum yields of films were measured with an integration sphere. Electrochemical behavior was investigated by cyclic voltammetry (CV) with a standard three-electrode electrochemical cell in a 0.1 M tetra-*n*-butylammonium hexafluorophosphate (Bu_4NPF_6) in nonaqueous acetonitrile at room temperature under nitrogen with a scanning rate of 50 mV s^{-1}. A platinum working electrode, a glassy carbon electrode, and an $Ag/AgNO_3$ (0.1 M) reference electrode were used. The CV curves were calibrated using ferrocene/ferrocenium (Fc/Fc^+) redox couple (4.8 eV below the vacuum level) as the internal standard. The formal potential of Fc/Fc^+ was measured as 0.09 V against Ag/Ag^+. Thus, the highest occupied molecular orbital (HOMO) and the lowest unoccupied molecular orbital (LUMO) energy levels could be calculated according to: $E_{HOMO} = -e(E_{ox} + 4.71\ V)$, $E_{LUMO} = -e(E_{red} + 4.71\ V)$; where E_{ox} and E_{red} is the onset oxidation and reduction potential, respectively. Differential scanning calorimetry (DSC) and thermo-gravimetric analysis (TGA) were done on Shimadzu DSC-60A and DTG-60A equipment, respectively. The surface morphology of the films was investigated by atomic force microscopy (AFM, Bruker Dimension Icon). The molecular structures of the **Py-*n*TAT** were optimized using density functional theory (DFT) method (B3LYP) with 6-31G (d) basis set by GAUSSIAN 09.

Device fabrication and measurements

Thin-film samples (100–225 nm thickness) for optical measurements (absorption and PL spectra, PLQY, PL decay, and ASE measurements) were prepared by spin-coating starburst solutions (comprising 35 mg mL^{-1} of **Py-2TAT** or 20 mg mL^{-1} of **Py-4TAT** in $CHCl_3$) onto precleaned spectrosil substrates. DFB lasers were fabricated by nanoimprint lithography (NIL) method and then **Py-2TAT** and **Py-4TAT** were spin-coated on top.

For ASE measurements, the samples were optically pumped with the pulsed (5 ns, 10 Hz, 355 nm) output of a Q-switched Nd:YAG laser pumped optical parametric amplifier (Spectron SL 450) focused with a cylindrical lens to form a 4 mm × 0.55 mm stripe-shaped excitation area on the sample. For DFB lasers, the pump excitation area employed for monitoring laser emission was a circular spot with 250 μm in diameter (4.9×10^{-4} cm^2 in area). The pulse energy incident on the sample was adjusted by the insertion of calibrated neutral density filters into the beam path. The laser emission was monitored with a fiber-coupled spectrograph and a charge coupled device (CCD) detector. The pump laser beam was incident on the sample at an angle of 45° to the surface normal in order to allow spatial separation at the CCD detector of the DFB laser output (emitted normal to the film plane) and reflected light from the strong pump.

Synthesis

3-Bromo-5,10,15-trihexyl-10,15-dihydro-5*H*-diindolo[3,2-*a*:3′,2′-*c*]carbazole (2). 5,10,15-Trihexyl-10,15-dihydro-5*H*-diindolo[3,2-*a*:3′,2′-*c*]carbazole (**TAT**) (**1**) (0.50 g, 0.85 mmol) in acetonitrile (20 mL) was stirred at 0 °C, and then *N*-bromosuccinimide (NBS) (0.25 g, 0.74 mmol) in 15 mL *N*,*N*-dimethylformamide (DMF) was added dropwise. The mixture was stirred at that temperature for 1 h and then stirred overnight at room temperature. The solvent

was evaporated under reduced pressure and the residue was extracted with dichloromethane (CH_2Cl_2). After CH_2Cl_2 was evaporated, the resulting crude product was purified by column chromatography, eluting with petroleum (PE)/CH_2Cl_2 (10 : 1) to get **2** as a white solid (0.35 g, 60%). MALDI-TOF MS (*m*/*z*): calcd for $C_{42}H_{50}BrN_3$, exact mass: 675.32, mol. wt.: 676.77; found: 675.46. ^{1}H NMR (400 MHz, $CDCl_3$): δ 8.25 (dd, 2H, J = 14.8, 8.0 Hz), 8.06 (d, 1H, J = 8.6 Hz), 7.72 (s, 1H), 7.62 (t, 2H, J = 7.1 Hz), 7.52–7.38 (m, 3H), 7.35 (t, 2H, J = 6.4 Hz), 4.93–4.74 (m, 6H), 1.96 (s, 6H), 1.47–1.09 (m, 18H), 0.82 (s, 9H). ^{13}C NMR (100 MHz, $CDCl_3$): δ 141.9, 141.0, 139.0, 138.4, 123.3, 122.4, 121.6, 119.7, 116.0, 113.3, 110.9, 103.1, 47.1, 31.4, 29.7, 26.2, 22.7, 14.1.

5,10,15-Trihexyl-3-(4,4,5,5-tetramethyl-1,3,2-dioxaborolan-2-yl)-10,15-dihydro-5*H*-diindolo[3,2-*a*:3′,2′-*c*]carbazole (3). In a 50 mL flame dried two-necked flask, **2** (1.07 g, 1.58 mmol), bis(pinacolato)diboron (0.75 g, 2.96 mmol), and $Pd(dppf)_2Cl_2$ (0.05 g, 0.05 mmol), anhydrous potassium acetate (4.44 g, 0.44 mmol) were added and subjected to three vacuum/nitrogen fill cycles. Nitrogen-degassed freshly distilled 1,4-dioxane was subsequently added. The mixture was stirred for 24 h at 100 °C. Water was added to quench the reaction and the organic layer was extracted with CH_2Cl_2. CH_2Cl_2 was subsequently removed under reduced pressure. The resulting crude product was purified by column chromatography, eluting with PE/CH_2Cl_2 (3 : 1) to produce compound **3** as a pale yellow oil (0.54 g, 51%). MALDI-TOF MS (*m*/*z*): calcd for $C_{48}H_{62}BN_3O_2$, exact mass: 723.49, mol. wt.: 723.84; found: 723.84. ^{1}H NMR (400 MHz, $CDCl_3$): δ 8.30 (d, 3H, J = 7.9 Hz), 8.11 (s, 1H), 7.81 (d, 1H, J = 8.0 Hz), 7.64 (d, 2H, J = 8.0 Hz), 7.46 (t, 2H, J = 7.5 Hz), 7.36 (d, 2H, J = 4.1 Hz), 5.03–4.96 (m, 6H), 4.96–4.87 (m, 6H), 2.13–1.89 (m, 12H), 1.46 (s, 18H), 0.95–0.74 (m, 9H). ^{13}C NMR (100 MHz, $CDCl_3$): δ 141.0, 140.9, 140.5, 139.6, 139.3, 138.9, 125.9, 123.5, 123.4, 122.7, 121.6, 121.4, 120.6, 119.7, 119.6, 116.9, 110.5, 110.4, 103.2, 83.7, 77.3, 77.0, 76.7, 47.1, 47.0, 31.5, 31.4, 31.3, 29.7, 26.4, 26.3, 26.2, 25.0, 22.5, 22.4, 13.9.

5,10,15-Trihexyl-2-(6-(5,10,15-trihexyl-10,15-dihydro-5*H*-diindolo[3,2-*a*:3′,2′-*c*]carbazol-3-yl)pyren-1-yl)-10,15-dihydro-5*H*-diindolo[3,2-*a*:3′,2′-*c*]carbazole (Py-2TAT). To a stirred solution of compound **3** (0.22 g, 0.5 mmol) in 1,4-dioxane (30 mL) was added 1,6-dibromopyrene (0.072 g, 0.2 mmol), potassium carbonate (0.83 g, 3 mmol), H_2O (10 mL), and $Pd(PPh_3)_4$ (28 mg, 0.025 mmol). The resulting mixture was stirred at 100 °C under nitrogen atmosphere for 36 h. The solvent was evaporated under reduced pressure and the residue was treated with water (80 mL), extracted with CH_2Cl_2. The organic layers were combined and washed twice with water and once with brine, dried over anhydrous magnesium sulfate. After removing the solvent under reduced pressure, the residue was purified by column chromatography, eluting with petroleum (PE)/CH_2Cl_2 (4 : 1) to afford **Py-2TAT** as a yellow-green solid (0.17 g, 60%). MALDI-TOF MS (*m*/*z*): calcd for $C_{100}H_{108}N_6$, exact mass: 1392.86, mol. wt.: 1393.97; found: 1394.28. ^{1}H NMR (400 MHz, $CDCl_3$): δ 8.47 (d, J = 9.4 Hz, 4H), 8.33 (t, J = 7.9 Hz, 6H), 8.24 (d, J = 7.8 Hz, 2H), 8.15 (d, J = 9.4 Hz, 2H), 7.92 (s, 2H), 7.68 (t, J = 7.7 Hz, 6H), 7.49 (dd, J = 14.4, 7.1 Hz, 4H), 7.37 (dd, J = 14.2, 7.0 Hz, 4H), 5.08–4.93 (m, 12H), 2.16–1.99 (m, 12H), 1.35–1.21 (m, 36H), 0.87–0.80 (m, 18H). ^{13}C NMR (100 MHz, $CDCl_3$): δ 141.2, 141.1, 141.0, 139.4, 139.0, 138.8, 138.7, 135.8, 130.4, 129.3, 127.3, 125.5, 124.8, 124.4, 123.8, 123.5, 123.4, 123.0, 122.7, 121.5, 121.2, 119.7, 112.7, 110.5, 103.3, 103.1, 77.3, 77.2, 77.0, 76.7, 47.1, 31.5, 31.4, 29.9, 29.8, 26.4, 26.3, 22.5, 22.4, 13.9.

1,3,6,8-Tetrakis(5,10,15-trihexyl-10,15-dihydro-5*H*-diindolo[3,2-*a*:3′,2′-*c*]carbazol-3-yl)pyrene (Py-4TAT). To a stirred solution of compound **3** (0.84 g, 1.16 mmol) in 1,4-dioxane (45 mL) was added 1,3,6,8-tetrabromopyrene (0.1 g, 0.19 mmol), potassium carbonate (0.83 g, 3 mmol), H_2O (15 mL), and $Pd(PPh_3)_4$ (28 mg, 0.025 mmol). The resulting mixture was stirred at 100 °C under nitrogen atmosphere for 36 h. The solvent was evaporated under reduced pressure and the residue was treated with water (80 mL), extracted with CH_2Cl_2. The organic layers were combined and washed twice with water and once with brine, dried over anhydrous magnesium sulfate. After removing the solvent under reduced pressure, the residue was purified by column chromatography, eluting with petroleum (PE)/CH_2Cl_2 (2 : 1) to afford **Py-4TAT** as a yellow solid (0.26 g, 54%). MALDI-TOF MS (*m*/*z*): calcd for $C_{184}H_{206}N_{12}$, exact mass: 2583.65, mol. wt.: 2585.68; found: 2583.92. ^{1}H NMR (400 MHz, $CDCl_3$): δ 8.59 (s, 4H), 8.56–8.46 (m, 6H), 8.32 (d, J = 7.9 Hz, 8H), 8.07 (s, 4H), 7.82 (d, J = 8.2 Hz, 4H), 7.66 (t, J = 7.7 Hz, 8H), 7.47 (dd, J = 15.1, 7.5 Hz, 8H), 7.36 (dd, J = 16.3, 8.2 Hz, 8H), 4.97 (dd, J = 22.9, 15.4 Hz, 24H), 2.16–1.97 (m, 24H), 1.25 (ddd, J = 29.4, 27.4, 17.1 Hz, 72H), 0.96–0.69 (m, 36H). ^{13}C NMR (100 MHz, $CDCl_3$): δ 141.3, 141.0, 139.4, 139.0, 138.8, 135.8, 130.5, 128.6, 126.5, 125.7, 123.5, 123.4, 122.8, 122.7, 121.5, 121.2, 119.7, 112.7, 110.5, 103.3, 103.1, 47.1, 34.7, 33.1, 31.5, 31.4, 29.9, 29.8, 26.9, 26.4, 26.3, 22.5, 22.4, 13.9, 13.8.

Acknowledgements

The authors acknowledge financial support from the National Key Basic Research Program of China (973 Program, 2014CB648300), the National Natural Science Foundation of China (21422402, 20904024, 51173081, 61136003), the Natural Science Foundation of Jiangsu Province (BK20140060, BK20130037, BM2012010), Program for Jiangsu Specially – Appointed Professors (RK030STP15001), Program for New Century Excellent Talents in University (NCET-13-0872), Specialized Research Fund for the Doctoral Program of Higher Education (20133223110008, and 20113223110005), the Ministry of Education of China (IRT1148), the Synergetic Innovation Center for Organic Electronics and Information Displays, the Priority Academic Program Development of Jiangsu Higher Education Institutions (PAPD), the NUPT "1311 Project", the Six Talent Plan (2012XCL035), the 333 Project (BRA2015374) and the Qing Lan Project of Jiangsu Province.

References

1 Y. Shirota and H. Kageyama, *Chem. Rev.*, 2007, **107**, 953–1010.
2 J. Wu, W. Pisula and K. Müllen, *Chem. Rev.*, 2007, **107**, 718–747.

3 P. Strohriegl and J. V. Grazulevicius, *Adv. Mater.*, 2002, **14**, 1439–1452.
4 P. L. Burn, S. C. Lo and I. D. W. Samuel, *Adv. Mater.*, 2007, **19**, 1675–1688.
5 A. L. Kanibolotsky, I. F. Perepichkaz and P. J. Skabara, *Chem. Soc. Rev.*, 2010, **39**, 2695–2728.
6 I. D. W. Samuel and G. A. Turnbull, *Chem. Rev.*, 2007, **107**, 1272–1295.
7 S. Chénais and S. Forget, *Polym. Int.*, 2012, **61**, 390–406.
8 S. Z. Bisri, T. Takenobu and Y. Iwasa, *J. Mater. Chem. C*, 2014, **2**, 2827.
9 B. K. Yap, R. Xia, M. Campoy-Quiles, P. N. Stavrinou and D. D. Bradley, *Nat. Mater.*, 2008, **7**, 376–380.
10 D. Amarasinghe, A. Ruseckas, A. E. Vasdekis, G. A. Turnbull and I. D. Samuel, *Adv. Mater.*, 2009, **21**, 107–110.
11 E. B. Namdas, M. Tong, P. Ledochowitsch, S. R. Mednick, J. D. Yuen, D. Moses and A. J. Heeger, *Adv. Mater.*, 2009, **21**, 799–802.
12 H. Kim, N. Schulte, G. Zhou, K. Müllen and F. Laquai, *Adv. Mater.*, 2011, **23**, 894–897.
13 X. F. Jiang, Y. F. Xiao, C. L. Zou, L. He, C. H. Dong, B. B. Li, Y. Li, F. W. Sun, L. Yang and Q. Gong, *Adv. Mater.*, 2012, **24**, 260–264.
14 M. M. Mróz, G. Sforazzini, Y. Zhong, K. S. Wong, H. L. Anderson, G. Lanzani and J. Cabanillas-Gonzalez, *Adv. Mater.*, 2013, **25**, 4347–4351.
15 B. Liu, W.-L. Yu, Y.-H. Lai and W. Huang, *Macromolecules*, 2000, **33**, 8945–8952.
16 B. Liu, W.-L. Yu, Y.-H. Lai and W. Huang, *Chem. Mater.*, 2001, **13**, 1984–1991.
17 G. Zeng, W.-L. Yu, S.-J. Chua and W. Huang, *Macromolecules*, 2002, **35**, 6907–6914.
18 C. W. Tang and S. VanSlyke, *Appl. Phys. Lett.*, 1987, **51**, 913–915.
19 J. Shi and C. W. Tang, *Appl. Phys. Lett.*, 2002, **80**, 3201–3203.
20 Y. H. Kim, H. C. Jeong, S. H. Kim, K. Yang and S. K. Kwon, *Adv. Funct. Mater.*, 2005, **15**, 1799–1805.
21 C. Tang, F. Liu, Y.-J. Xia, J. Lin, L.-H. Xie, G.-Y. Zhong, Q.-L. Fan and W. Huang, *Org. Electron.*, 2006, **7**, 155–162.
22 C. Tang, F. Liu, Y.-J. Xia, L.-H. Xie, A. Wei, S.-B. Li, Q.-L. Fan and W. Huang, *J. Mater. Chem.*, 2006, **16**, 4074–4080.
23 T. M. Figueira-Duarte and K. Müllen, *Chem. Rev.*, 2011, **111**, 7260–7314.
24 S. Krotkus, K. Kazlauskas, A. Miasojedovas, A. Gruodis, A. Tomkeviciene, J. V. Grazulevicius and S. Jursenas, *J. Phys. Chem. C*, 2012, **116**, 7561–7572.
25 L. Ji, Q. Fang, M. S. Yuan, Z. Q. Liu, Y. X. Shen and H. F. Chen, *Org. Lett.*, 2010, **12**, 5192–5195.
26 T. Bura, N. Leclerc, R. Bechara, P. Lévêque, T. Heiser and R. Ziessel, *Adv. Energy Mater.*, 2013, **3**, 1118–1124.
27 C. Ruiz, J. T. López Navarrete, M. C. Ruiz Delgado and B. Gómez-Lor, *Org. Lett.*, 2015, **17**, 2258.
28 A. Benito-Hernández, U. K. Pandey, E. Cavero, R. Termine, E. M. García-Frutos, J. L. Serrano, A. Golemme and B. Gómez-Lor, *Chem. Mater.*, 2013, **25**, 117–121.
29 T. Bura, N. Leclerc, S. Fall, P. Lévêque, T. Heiser and R. Ziessel, *Org. Lett.*, 2011, **13**, 6030–6033.
30 J. Shao, Z. Guan, Y. Yan, C. Jiao, Q.-H. Xu and C. Chi, *J. Org. Chem.*, 2011, **76**, 780–790.
31 W. Y. Lai, Q. Y. He, R. Zhu, Q. Q. Chen and W. Huang, *Adv. Funct. Mater.*, 2008, **18**, 265–276.
32 W. Y. Lai, Q. Q. Chen, Q. Y. He, Q. L. Fan and W. Huang, *Chem. Commun.*, 2006, 1959–1961.
33 W. Y. Lai, R. Zhu, Q. L. Fan, L. T. Hou, Y. Cao and W. Huang, *Macromolecules*, 2006, **39**, 3707–3709.
34 R. Zhu, W.-Y. Lai, H.-Y. Wang, N. Yu, W. Wei, B. Peng, W. Huang, L.-T. Hou, J.-B. Peng and Y. Cao, *Appl. Phys. Lett.*, 2007, **90**, 141909.
35 W. Y. Lai, R. Xia, Q. Y. He, P. A. Levermore, W. Huang and D. D. Bradley, *Adv. Mater.*, 2009, **21**, 355–360.
36 W. Y. Lai, R. Xia, D. D. Bradley and W. Huang, *Chem.–Eur. J.*, 2010, **16**, 8471–8479.
37 T. Qin, W. Wiedemair, S. Nau, R. Trattnig, S. Sax, S. Winkler, A. Vollmer, N. Koch, M. Baumgarten, E. J. List and K. Mullen, *J. Am. Chem. Soc.*, 2011, **133**, 1301–1303.
38 V. de Halleux, J. P. Calbert, P. Brocorens, J. Cornil, J. P. Declercq, J. L. Brédas and Y. Geerts, *Adv. Funct. Mater.*, 2004, **14**, 649–659.
39 M. Franceschin, L. Ginnari-Satriani, A. Alvino, G. Ortaggi and A. Bianco, *Eur. J. Org. Chem.*, 2010, **2010**, 134–141.
40 R. Muangpaisal, M.-C. Ho, T.-H. Huang, C.-H. Chen, J.-Y. Shen, J.-S. Ni, J. T. Lin, T.-H. Ke, L.-Y. Chen, C.-C. Wu and C. Tsai, *Org. Electron.*, 2014, **15**, 2148–2157.
41 G. Zhang, M. Baumgarten, M. Auer, R. Trattnig, E. J. List-Kratochvil and K. Mullen, *Macromol. Rapid Commun.*, 2014, **35**, 1931–1936.
42 R. D. Xia, W. Y. Lai, P. A. Levermore, W. Huang and D. D. C. Bradley, *Adv. Funct. Mater.*, 2009, **19**, 2844–2850.
43 A. G. Crawford, A. D. Dwyer, Z. Liu, A. Steffen, A. Beeby, L.-O. Pålsson, D. J. Tozer and T. B. Marder, *J. Am. Chem. Soc.*, 2011, **133**, 13349–13362.
44 T. Oyamada, S. Akiyama, M. Yahiro, M. Saigou, M. Shiro, H. Sasabe and C. Adachi, *Chem. Phys. Lett.*, 2006, **421**, 295–299.
45 M. Gingras, V. Placide, J. M. Raimundo, G. Bergamini, P. Ceroni and V. Balzani, *Chem.–Eur. J.*, 2008, **14**, 10357–10363.
46 T. Brown, J. Kim, R. Friend, F. Cacialli, R. Daik and W. Feast, *Appl. Phys. Lett.*, 1999, **75**, 1679–1681.
47 N. Tessler, *Adv. Mater.*, 1999, **11**, 363–370.
48 E. M. Calzado, P. G. Boj and M. A. Díaz-García, *Int. J. Mol. Sci.*, 2010, **11**, 2546–2565.
49 L. Cerdán, A. Costela, G. Durán-Sampedro, I. García-Moreno, M. Calle, M. Juan-y-Seva, J. de Abajo and G. A. Turnbull, *J. Mater. Chem.*, 2012, **22**, 8938–8947.
50 A. Miasojedovas, K. Kazlauskas, G. Armonaite, V. Sivamurugan, S. Valiyaveettil, J. Grazulevicius and S. Jursenas, *Dyes Pigm.*, 2012, **92**, 1285–1291.